Acta Crystallographica Section D
Biological Crystallography
ISSN 0907-4449

Mycobacterium tuberculosis acyl carrier protein synthase adopts two different pH-dependent structural conformations

Kuppan Gokulan,[a] Anup Aggarwal,[a] Lance Shipman,[a]‡ Gurdyal S. Besra[b] and James C. Sacchettini[a]*

[a]Department of Biochemistry and Biophysics, Texas A&M University, College Station, TX 77843-3474, USA, and [b]School of Biosciences, University of Birmingham, Edgbaston, Birmingham B15 2TT, England

‡ Present address: Department of Chemistry, Morehouse College, Atlanta, GA 30314, USA.

Correspondence e-mail: sacchett@tamu.edu

Received 5 January 2011
Accepted 26 May 2011

PDB References:
M. tuberculosis apo-AcpS, 3ne3; with sulfate ion, 3ne1; *C. ammoniagenes* apo-AcpS, 3ne9; AcpS–CoA complex, 3nfd.

The crystal structures of acyl carrier protein synthase (AcpS) from *Mycobacterium tuberculosis* (*Mtb*) and *Corynebacterium ammoniagenes* determined at pH 5.3 and pH 6.5, respectively, are reported. Comparison of the *Mtb* apo-AcpS structure with the recently reported structure of the *Mtb* AcpS–ADP complex revealed that AcpS adopts two different conformations: the orthorhombic and trigonal space-group structures show structural differences in the α2 helix and in the conformation of the α3–α4 connecting loop, which is in a closed conformation. The apo-AcpS structure shows electron density for the entire model and was obtained at lower pH values (4.4–6.0). In contrast, at a higher pH value (6.5) AcpS undergoes significant conformational changes, resulting in disordered regions that show no electron density in the AcpS model. The solved structures also reveal that *C. ammoniagenes* AcpS undergoes structural rearrangement in two regions, similar to the recently reported *Mtb* AcpS–ADP complex structure. *In vitro* reconstitution experiments show that AcpS has a higher post-translational modification activity between pH 4.4 and 6.0 than at pH values above 6.5, where the activity drops owing to the change in conformation. The results show that apo-AcpS and AcpS–ADP adopt different conformations depending upon the pH conditions of the crystallization solution.

1. Introduction

The fatty-acid synthase type I (FAS-I) pathway is widely present in eukaryotes (Smith, 1994) and consists of a single large polypeptide containing multiple active centers. The fatty-acid synthase type II (FAS-II) pathway is present in all bacteria and plants and comprises a system in which discrete monofunctional enzymes encoded by specific genes carry out each reaction in the pathway (Magnuson *et al.*, 1993). Fatty-acid biosynthesis is more complicated in *Mycobacteria* and *Corynebacteria* species compared with other bacteria owing to the presence of both the FAS-I and FAS-II pathways.

Lipid biosynthesis is essential to the survival of *M. tuberculosis* (*Mtb*) (Taylor *et al.*, 2010). There are two important components in fatty-acid biosynthesis, CoAs and acyl carrier proteins (ACPs), both of which are essential for priming and extending the growing acyl chain. Apo-ACP is post-translationally modified by the transfer of a 4′-phosphopantetheine (4′-ppt) prosthetic group from coenzyme A to holo-ACP by acyl carrier protein synthase (AcpS). In both the FAS-I and FAS-II pathways the fatty acids are synthesized by repeated cycles of reactions, namely the transacylation,

© 2011 International Union of Crystallography
Printed in Singapore – all rights reserved

condensation, dehydration and reduction reactions (Rock & Cronan, 1996).

The AcpS enzyme was initially identified and characterized in *Escherichia coli*, in which it is an essential enzyme for bacterial growth (Lambalot & Walsh, 1995). The *Mtb* genome contains two phosphopantetheine transferases: AcpS and 4′-phosphopantetheinyl transferase (PptT; Cole *et al.*, 1998). Both enzymes are essential for bacterial survival and synthesis of virulence factors (Chalut *et al.*, 2006). AcpS is predominantly associated with the biosynthesis of fatty acids in both FAS systems, but it is also involved in polyketide synthesis (Shen *et al.*, 1992), nonribosomal peptide synthesis (Baldwin *et al.*, 1991), transacylation of oligosaccharides (Geiger *et al.*, 1991) and protein synthesis (Issartel *et al.*, 1991). A recent study showed that AcpS is predominately associated with post-translational modification of FAS-I and the AcpM subunit of the FAS-II system (Chalut *et al.*, 2006). In contrast, the PptT enzyme is involved in post-translational modification of type I polyketide synthase enzymes. The *Mtb* genome contains more than 18 type I polyketide synthase enzymes (Cole *et al.*, 1998), which catalyze the biosynthesis of phenolic lipids (Dubey *et al.*, 2003) in virulent strains. In the type II synthase, the hydrophobic fatty-acyl intermediates sequentially shuttle between enzymes through an ACP. All acyl chains undergoing biosynthesis by FAS are attached to the terminal cysteine thiol of 4′-ppt *via* a labile thioester bond, making AcpS an essential enzyme. In addition, the 4′-ppt prosthetic group has a long flexible arm that can reach into the active site of enzymes, where the sulfhydryl group is available for the attachment of an acyl group. The divalent Mg^{2+} ion is required for the post-translational modification reaction and is essential for the biosynthesis of all bacterial fatty acids, several bacterial lipopolysaccharides and membrane lipids. Recently, it has been reported that the AcpS gene product is essential for the growth of *Streptococcus pneumoniae* (McAllister *et al.*, 2000). The nature of FAS-II in bacteria is quite different from the mammalian lipid-biosynthetic pathway and provides various specific sites for selective inhibition by antibacterial agents. Furthermore, AcpS is widely present in *Mycoplasma*, Gram-positive and Gram-negative bacteria; thus, an AcpS inhibitor could alter the availability of holo-ACP for the acylation process and the availability of components for fatty-acid biosynthesis, making such inhibitors possible broad-spectrum antibacterial agents. In the past ten years, structures of AcpS have been solved for several pathogenic bacteria (Table 1), including *Streptomyces coelicolor* (PDB entry 2wdo; P. Dall'Aglio, C. Arthur, M. P. Crump, J. Crosby & A. T. Hadfield, unpublished work), *Streptococcus pneumoniae* (PDB entry 1fte; Chirgadze *et al.*, 2000), *Bacillus subtilis* (PDB entry 1f80; Parris *et al.*, 2000), *B. anthracis* (PDB entry 3hyk; Center for Structural Genomics of Infectious Diseases, unpublished work) and *Mycobacterium smegmatis* (PDB entry 3gwm; C. Poulsen, M. Wilmanns & Y. H. Song, unpublished work), revealing the role of this enzyme in post-translational modification.

We report here the crystal structures of *C. ammoniagenes* AcpS (with and without CoA) and *Mtb* apo-AcpS. *Mtb* apo-AcpS has an overall structure similar to those of the recently reported *Mtb* AcpS–ADP complex and the *C. ammoniagenes* AcpS structure described here. Despite their overall similarity, the two structures exhibit significant conformational changes in the α-carbon backbone. *Mtb* AcpS was crystallized both at low pH values (4.4–6.0) and higher pH values (6.5 and 7.5); interestingly, AcpS showed higher post-translational modification activity at the lower pH. The *Mtb* and *C. ammoniagenes* AcpS structures suggest that pH may play a significant role in conformational change but that CoA binding has no effect on the structural rearrangement. The transfer of the 4′-ppt moiety from CoA to the Asp-Ser-Leu (DSL) motif of the mycobacterial ACP (AcpM) is likely to require the association of AcpS and apo-AcpM. To understand the interaction between these two proteins, the *Mtb* AcpS and *Mtb* ACP NMR structures (PDB entry 1klp; Wong *et al.*, 2002) were superimposed on the *B. subtilis* AcpS–ACP complex. The superimposed model of *Mtb* AcpS–ACP shows that the conserved DSL motif of AcpM occupies a dimer interface of AcpS and is in close enough proximity to interact with either 3′,5′-ADP or CoA.

Table 1
List of AcpS structures from several pathogenic bacteria and their sequence similarity to *Mtb* AcpS.

Bacterium	PDB entry	Sequence similarity to *Mtb* AcpS (%)	R.m.s.d. (Å)
Streptomyces coelicolor	2wdo	39	1.58
Mycobacterium smegmatis	3gwm	84	1.07
Bacillus anthracis	3hyk	32	2.07
Staphylococcus aureus	3f09	26	2.12
Streptococcus pneumoniae	1fte	27	2.18
Bacillus subtilis	1f80	29	1.98

2. Materials and methods

2.1. Cloning, expression and purification of *C. ammoniagenes* AcpS and *Mtb* AcpS

A 0.45 kb DNA fragment containing the AcpS gene was amplified by PCR using *C. ammoniagenes* genomic DNA as the template (forward primer, 5′-CATATGCTCGACAACCGTGAAGCG; reverse primer, 5′-AAGCTTTTACCGCAGGTACCGCAG). The amplified DNA fragment was digested with *Nde*I and *Hin*dIII and subcloned into the corresponding restriction sites in the pET28a vector to yield N-terminally His_6-tagged AcpS. *E. coli* B834 (DE3) Met cells were transformed with the AcpS-pET28a/His vector. For the production of SeMet-incorporated protein the cells were grown in M9 minimal medium supplemented with all 19 standard amino acids and selenomethionine. Expression of AcpS was induced with 1 m*M* IPTG and cells were harvested after 6 h of growth at 289 K.

A 0.4 kb DNA fragment containing the AcpS gene (Rv2523c; Swiss-Prot accession No. O53228) was amplified by PCR using *Mtb* H37Rv genomic DNA as the template (forward primer, 5′-ATGGGCATCGTCGGTGTGGG; reverse primer, 5′-TCACGGGGCCTCCAGGATGGCGAC). The

amplified DNA fragment was digested with *Nco*I and *Bam*HI and subcloned into the corresponding restriction sites in the pET28a vector to yield C-terminally His_6-tagged AcpS. The AcpS-pET28a vector was transformed into *E. coli* BL21 (DE3) cells by heat-shock transformation. The transformed cells were grown to mid-log exponential phase at 310 K in Terrific Broth medium containing kanamycin. Expression of AcpS was induced with 1 m*M* IPTG and cells were harvested after 6 h of growth at 289 K.

The harvested cell pellet was resuspended in buffer *A* (20 m*M* Tris–HCl pH 8.0, 100 m*M* imidazole, 0.5 *M* NaCl) with 1 m*M* PMSF and Complete EDTA-free protease-inhibitor cocktail (Roche). The cell lysate was disrupted by three passages through a cooled French pressure cell and repeatedly sonicated at 277 K with 30 s pulses. The resulting cell extract was centrifuged at 15 000*g* at 277 K for 1 h. The cleared supernatant was loaded onto a Hi-Trap Ni^{2+}-chelating column (Pharmacia Biosciences) and washed with 300 ml buffer *A*. His-tagged AcpS was eluted with a 100 ml linear gradient of 100–500 m*M* imidazole in 20 m*M* Tris–HCl pH 8.0 and 0.5 *M* NaCl. After purification to near-homogeneity by size-exclusion chromatography on a Superdex G-75 gel-filtration column (Pharmacia Biosciences), AcpS was dialyzed against 20 m*M* Tris–HCl pH 8.0 buffer, concentrated to 8 mg ml^{-1} and stored in 20 m*M* Tris–HCl pH 8.0 at 193 K.

2.2. Cloning, expression and purification of *Mtb* ACP (AcpM)

A 0.35 kb DNA fragment containing the ACP gene (Rv2244; Uni-Prot accession No. POA4W6) was amplified by PCR from *Mtb* H37Rv genomic DNA (forward primer, 5′-AAGAAGAGGCGGCCGCATGCCTGTCACTCAGGA-GCCTGTCACTCAGGAAGA; reverse primer, 5′-AAGAA-GAGCCATGCCTTGGACTCGGCCTCAAGCCTC).

The amplified DNA fragment was digested with *Not*I and *Nco*I and subcloned into the corresponding restriction sites in the pET30b vector to yield C-terminally His_6-tagged AcpM. The AcpM-pET30b vector was transformed into *E. coli* BL21 (DE3) cells. The transformed cells were grown to mid-log phase at 310 K in Terrific Broth containing kanamycin. Expression of AcpM was induced with 1 m*M* IPTG and cells were harvested after 6 h of growth at 289 K.

The harvested cell pellet was resuspended in buffer *A* (20 m*M* Tris–HCl pH 8.0, 10 m*M* imidazole, 0.5 *M* NaCl) with 1 m*M* PMSF and Complete EDTA-free protease-inhibitor cocktail (Roche). The cell lysate was disrupted by three passages through a cooled French pressure cell and repeatedly sonicated at 277 K with 30 s pulses. The resulting cell extract was centrifuged at 15 000*g* at 277 K for 1 h. The cleared supernatant was loaded onto a Hi-Trap Ni^{2+}-chelating column (Pharmacia Biosciences) and washed with 300 ml buffer *A*. His-tagged AcpM was eluted with a 200 ml linear gradient of 10–500 m*M* imidazole in 20 m*M* Tris–HCl pH 8.0 and 0.5 *M* NaCl. The peak fractions were pooled and dialyzed against 20 m*M* Tris buffer pH 8.0. The concentrated protein was stored at 193 K until use.

2.3. AcpS post-translational modification fluorescence assay

The 4′-ppt transferase activity of AcpS was assessed using BODIPY-labeled CoA. For this purpose, BODIPY-S-CoA was synthesized using CoA (Sigma) and BODIPY FL *N*-(2-aminoethyl)maleimide (Invitrogen; La Clair *et al.*, 2004). In the assay, 50 µ*M* AcpM was incubated with either 0.2 or 2 µ*M* AcpS for 1 h at room temperature in the dark in 20 m*M* HEPES pH 7.5 buffer containing 10 µl BODIPY-S-CoA (60 µ*M* final concentration) and 10 m*M* $MgCl_2$. As a control, AcpM was also pre-incubated with AcpS and 300 µ*M* CoA for 1 h at room temperature in the dark before the addition of BODIPY-S-CoA to the reaction mixture. PKS11 was used as a negative control as it is not a substrate of AcpS *in vivo*. PKS11 was incubated with BODIPY-S-CoA in the presence of AcpS, as performed for AcpM. After incubation, the reactions were stopped by the addition of 20% TCA to the mixture. The samples were incubated on ice for 15 min and then spun at 13 000*g* for 10 min. The supernatant was decanted and the pellets were washed twice with 200 µl ice-cold acetone. The pellets were dried in a speed vacuum, dissolved in a small amount of buffer and analyzed by SDS–PAGE. The resulting bands were analyzed under a UV-light scanner. The 4′-ppt transferase activity of AcpS was also measured at different pH values (3.4–8.0) using BODIPY-labeled CoA.

2.4. Crystallization and data collection

Initial crystallization conditions were screened by the hanging-drop method using a sparse-matrix kit (Crystal Screen and Crystal Screen 2, Hampton Research, California, USA; McPherson, 1982). *C. ammoniagenes* AcpS alone produced diffraction-quality crystals (space group $P2_12_12_1$) in 4–8 d at 291 K from 4 µl hanging drops consisting of a 1:1 ratio of AcpS (8 mg ml^{-1} concentration) and crystallization buffer consisting of 100 m*M* MES buffer pH 6.5, 0.2 *M* ammonium sulfate and 30%(*w*/*v*) PEG MME 5K. AcpS–CoA crystals were also obtained by the hanging-drop method. Protein solution (10 mg ml^{-1}) was mixed with an equal volume of precipitant solution to create 4 µl drops and incubated at 291 K. For protein crystals complexed with ligands, 0.5–2 m*M* CoA and 10 m*M* magnesium chloride were pre-incubated with AcpS for 10 min at room temperature. The precipitant solution for AcpS–CoA crystals consisted of 25%(*w*/*v*) PEG MME 5K, 0.1 *M* MES buffer pH 6.5 and 200 m*M* ammonium sulfate. The *C. ammoniagenes* AcpS–CoA complex crystallized in space group *P*1 with two trimers in the asymmetric unit.

The crystallization screen for *Mtb* AcpS was set up in hanging drops using the factorial screening method. Initial crystallization screening was carried out with AcpS alone in 10 m*M* $MgCl_2$ and 14 m*M* KCl (24 h at 277 K). Diffraction-quality crystals were obtained at 291 K when drops (1:1 ratio of protein:reservoir solution) were equilibrated against 500 µl well solution consisting of 5.6%(*w*/*v*) PEG 4K, 0.07 *M* sodium acetate pH 4.6–5.5, 50 m*M* ammonium sulfate and 30%(*v*/*v*) glycerol. The crystal belonged to space group *I*222, with unit-cell parameters a = 83.12, b = 104.87, c = 105.19 Å, and contained one homotrimer per asymmetric unit. Diffraction-

quality crystals were obtained after 3–4 d. Crystals belonging to space group *R*3 were obtained by the same method using a well solution consisting of 5.6% PEG 4K, 0.07 *M* sodium acetate pH 5.0–5.6, 50 m*M* ammonium acetate, 15% glycerol and 100 m*M* sodium iodide. The *R*3 crystals contained one molecule in the asymmetric unit.

Table 2
Anomalous data-collection and phasing statistics for *C. ammoniagenes* apo-AcpS.

(*a*) Data collection. Values in parentheses are for the highest resolution bin.

	Inflection (maximum f')	Peak (maximum f'')	High remote
Wavelength (Å)	0.979	0.979	0.963
Resolution range (Å)	99.0–2.48	99.0–2.48	99.0–2.48
Completeness (%)	100 (100)	100 (100)	100 (100)
Completeness, 2σ (%)	86 (67)	83 (56)	94 (85)
$\langle I/\sigma(I)\rangle$	13.7 (2.8)	15.9 (2.6)	23.1 (7.2)
$R_{\rm merge}$	0.10 (0.31)	0.10 (0.32)	0.09 (0.35)
f' (e$^-$)	−11.03	−8.49	−4.93
f'' (e$^-$)	3.20	5.28	3.44

(*b*) Phasing statistics.

Resolution bin (lower limit) (Å)	8.53	5.42	4.25	3.61	3.19	2.89	2.66	2.48
FOM initial (*SOLVE*)	0.61	0.40	0.36	0.31	0.23	0.17	0.12	0.10
FOM final (*SHARP*, DM NCS averaging)	0.79	0.49	0.42	0.29	0.17	0.12	0.10	0.70

A multi-wavelength anomalous dispersion data set for the *C. ammoniagenes* SeMet apo-AcpS crystal was collected on beamline 14-BM-D at the Advanced Photon Source (APS), Argonne National Laboratory using an Area Detector Systems Corporation Q4 area detector. High-resolution data sets for *C. ammoniagenes* AcpS–CoA and native AcpS crystals were collected on beamline 14-BM-C at APS. PEG 400 was used as a cryoprotectant for both apo-AcpS and the AcpS–CoA complex. The crystals were flash-frozen in a liquid-nitrogen stream at 120 K. *Mtb* apo-AcpS crystals (space groups *I*222 or $I2_12_12_1$ and *R*3) were captured in cryoloops and flash-cooled in an N_2 stream after brief soaks in mother liquor containing 20% ethylene glycol as a cryoprotectant. The data were reduced using *DENZO* (Otwinowski & Minor, 1997) and intensities were scaled with *SCALEPACK* (Otwinowski & Minor, 1997). Integrated and scaled data were analyzed by *XPREP* and indicated that the *Mtb* apo-AcpS crystals belonged to space group *I*222 or $I2_12_12_1$. Solvent-content calculations (Matthews, 1968) indicated the presence of a homotrimer ($V_{\rm M}$ = 2.55 Å^3 Da^{-1}, $V_{\rm S}$ = 51.76%) in the asymmetric unit. Molecular replacement (MR) in space group *I*222 gave a higher correlation coefficient (74.4%) and lower *R* factor (39.3%) compared with space group $I2_12_12_1$ (correlation coefficient of 34.2% and *R* factor of 58.9%). Therefore, *I*222 was the correct space group. The crystallographic data-collection statistics and refinement parameters are summarized in Tables 2 and 3.

Table 3
Data-collection, refinement and geometry statistics.

Values in parentheses are for the highest resolution bin.

	Mtb apo-AcpS		*C. ammoniagenes*	
			Apo AcpS	AcpS–CoA
Space group	*I*222	*R*3	$P2_12_12_1$	*P*1
Unit-cell parameters				
a (Å)	83.12	67.89	51.40	54.78
b (Å)	104.87	67.89	59.00	56.02
c (Å)	105.19	83.94	153.56	88.28
α (°)	90.00	90.00	90.00	80.88
β (°)	90.00	90.00	90.00	76.23
γ (°)	90.00	120.00	90.00	60.92
No. of crystals	1	1	2	1
Resolution (Å)	30–2.51 (2.60–2.51)	30–1.90 (1.95–1.90)	30–2.48 (2.48–2.50)	30–1.89 (1.95–1.89)
Unique reflections	15471 (1254)	6051 (855)	16881 (2038)	52264 (5869)
Completeness (%)	95.7 (75.5)	100 (100)	94.7 (78.6)	73 (51.0)
$R_{\rm merge}$	0.03 (0.14)	0.03 (0.19)	0.05 (0.15)	0.05 (0.18)
$\langle I/\sigma(I)\rangle$	13.83 (1.22)	54.00 (4.00)	17.35 (7.01)	58.10 (7.30)
Free *R* value (random 5%)	0.30 (0.35)	0.27 (0.38)	0.27 (0.28)	0.25 (0.29)
R value	0.23 (0.36)	0.24 (0.39)	0.20 (0.21)	0.21 (0.21)
No. of protein residues	387	129	399	804
B factor (Å^2)	74.14	43.75	30.14	24.91
Wavelength (Å)	1.54	0.97	0.97	0.97
No. of ADPs	0	0	0	6
No. of sulfates	4	0	4	0
R.m.s.d. bond lengths (Å)	0.03	0.03	0.02	0.031
R.m.s.d. bond angles (°)	1.48	1.66	1.64	2.036
Overall coordinate error (Å)	0.30	0.28	0.23	0.26
Real-space CC (*REFMAC*5)	0.94	0.94	0.92	0.93
Ramachandran plot, residues in				
Most favored region	332 [87.30%]	338 [88.70%]	387 [96.99%]	774 [96.27%]
Allowed region	45 [12.0%]	41 [10.7%]	7 [1.75%]	17 [2.11%]
Generously allowed region	3 [0.7%]	2 [0.3%]	0	0
Disallowed region	0	1 [0.3%]	5 [1.25%]	13 [1.62%]

2.5. Structure determination

The experimental phases for the *C. ammoniagenes* apo-AcpS structure were obtained by multi-wavelength anomalous dispersion phasing (Hendrickson & Ogata, 1997). *SHELXD* (Sheldrick, 2008) located three selenium sites in the asymmetric unit consistent with a homotrimer in the asymmetric unit and *SOLVE* (Terwilliger & Berendzen, 1999) was used to refine the sites and calculate the initial protein phase, resulting in an overall figure of merit of 0.7 (Table 2) for data in the resolution range 100–2.48 Å. The heavy-atom parameters were then refined and the phase was calculated in *SHARP* (de La Fortelle & Bricogne, 1997). Further phase improvement with solvent flattening in *autoSHARP* (Bricogne *et al.*, 2002) resulted in high-quality density-modified maps showing clear electron density for the correct hand for three molecules of protein in the

asymmetric unit. The initial protein model was built using *XFIT* (McRee, 1999) and a final high-quality model was produced after several cycles of manual model building and NCS-restrained maximum-likelihood refinement with *REFMAC*5 (Murshudov *et al.*, 2011) against the high-remote data set (Table 3). Water molecules were manually added during iterative cycles of building and refinement.

The structure of the *C. ammoniagenes* AcpS–CoA binary complex was solved by molecular replacement with *EPMR* (Kissinger *et al.*, 1999) using the final model of *C. ammoniagenes* apo-AcpS as the search model for data extending from 25 to 3.5 Å resolution. After model building and fitting, bias-minimized electron-density maps were obtained using the *Shake&wARP* protocol (Kantardjieff *et al.*, 2002). Clear electron density for CoA molecules was visible in the *Shake&wARP* map prior to any model building. After repeated cycles of refinement and manual model building, water molecules were added to the structure using *XFIT* (McRee, 1999; Table 3).

The structure of *Mtb* apo-AcpS was solved by molecular replacement with *EPMR*, giving a correlation coefficient of 0.45, using the final *C. ammoniagenes* apo-AcpS model as the search model for data extending from 25 to 3.5 Å resolution. The initial molecular-replacement model was mutated according to the *Mtb* AcpS sequence and manually rebuilt using *XFIT* into bias-minimized multiple-averaged electron-density maps obtained from the *Shake&wARP* map server. The initial electron-density map allowed the construction of a model with 129 residues (residues 2–130) in each subunit. Rigid-body refinement was carried out using *REFMAC*5. After repeated cycles of refinement and manual building, water molecules were added to the structure using *XFIT* (McRee, 1999). The final model has a crystallographic *R* factor of 23% and an $R_{\rm free}$ of 30% to a resolution of 2.51 Å with good stereochemistry (Table 3). *Mtb* apo-AcpS also crystallized in space group *R*3 with one molecule in the asymmetric unit. The *R*3 crystal structure was solved by molecular replacement using a single chain from the final model of *Mtb* apo-AcpS solved in space group *I*222. Several cycles of manual model building and likelihood refinement in *REFMAC*5 yielded a final 1.9 Å resolution model for the *R*3 crystal (Table 3). Water molecules were manually added during iterative cycles of building and refinement.

3. Results and discussion

The initial phases for the *C. ammoniagenes* apo-AcpS crystal diffraction data were obtained by MAD (Hendrickson, 1991) using crystals of selenomethionyl protein in space group $P2_12_12_1$. The unit-cell parameters and scaling with diffraction amplitudes showed that the AcpS–CoA binary complex crystallized in space group *P*1 with two trimers in the asymmetric unit. The initial map allowed the construction of a model with 136 residues in each subunit. The crystal structure of AcpS from *C. ammoniagenes* revealed that it assembles as a tightly packed homotrimer. The final structure consists of residues 5–47 and 61–153 (Fig. 1*a*) in three subunits designated *A*, *B* and *C*. The three polypeptide chains can be superimposed with r.m.s.d.s of 0.43 Å between chains *A* and *B* and of 0.53 Å between chains *A* and *C*. In an experimental map and in an unbiased electron-density map of native *C. ammoniagenes* AcpS the structure shows no electron density for the four N-terminal residues (1–4) or for residues 48–60 (the $\alpha2$–$\alpha3$ connecting loop). The *C. ammoniagenes* apo-AcpS structure has an α/β-fold (Fig. 1*a*) similar to those of the *B. subtilis* and *S. pneumoniae* AcpS structures (Chirgadze *et al.*, 2000; Parris *et al.*, 2000). The main core of the protein is the long $\alpha3$ helix. One side of the $\alpha3$ helix is covered by antiparallel β-sheets (consisting of $\beta1$, $\beta4$ and $\beta5$), while the other side of the helix is covered by a β-sheet composed of strands $\beta2$, $\beta3$ and $\beta4$ together with $\alpha1$ and $\alpha2$.

The *C. ammoniagenes* AcpS–CoA binary complex structure was solved by molecular replacement using the coordinates of the *C. ammoniagenes* apo-AcpS structure as a starting model. The crystallographic data-collection statistics and refinement parameters are summarized in Table 3. To obtain the molecular-replacement solution for *Mtb* AcpS, we used the coordinates of *C. ammoniagenes* AcpS as an initial search model. The structural data reveal that native *Mtb* AcpS (Fig. 1*b*) assembles as a tightly packed homotrimer and each subunit consists of residues 2–130.

AcpS forms a homotrimer in which the polypeptide chain is folded into four α-helices and five β-strands and trimerization is mediated through the residues of the antiparallel β-strands ($\beta1$, $\beta4$ and $\beta5$) of all three subunits. The three antiparallel β-strands of each subunit are arranged together and form a tunnel-like structure at the center of the trimer that runs through the entire length of the protein (Figs. 1*a* and 1*b*). The tunnel contains mainly hydrophobic residues that stabilize the biological unit, with intersubunit interactions occurring predominantly between the $\beta1$ strand of one subunit and the $\beta4$ strand of another subunit. The active site of AcpS is formed at the intermolecular interface between two subunits, specifically where the β-sheets of two AcpS molecules intersect in the trimer. The amino acids from one subunit surround one half of the active site and those from the second subunit surround the other half. Examination of the active site of the *C. ammoniagenes* native AcpS structure reveals a bowl-shaped depression (Figs. 1*a* and 1*b*) that is surrounded by charged residues and bound ordered water molecules. In the *C. ammoniagenes* and *Mtb* AcpS native structures the active sites are occupied by sulfate ions (Figs. 1*c* and 1*d*). In addition, hydrophobic residues create a hydrophobic tunnel for the 4′-ppt moiety.

3.1. Sequence and structural comparison of *Mtb* AcpS and *C. ammoniagenes* AcpS with other bacterial AcpSs

Multiple sequence alignments of known AcpS sequences are presented in Fig. 2 and show that *Mtb* AcpS has a lower sequence identity to *B. subtilis* AcpS and *S. pneumoniae* AcpS (29 and 27%, respectively) than to *C. ammoniagenes* AcpS, which displays 34% sequence identity to the homologous enzyme. The KEA*XX*KA motif, containing the Lys62 residue,

is within hydrogen-bonding distance of the 5′-phosphate and is conserved in the prokaryotic AcpS enzymes; the S*XXX*H motif interacts with either the 3′-phosphate of CoA or with ADP. Other conserved motifs include G*X*D (involved in chelating the Mg^{2+} ion), and RW and GRP, which are part of the CoA-binding regions. The RR*X*A and S*XXX*H sequence motifs are not conserved in the prokaryotic AcpS and surfactin synthetase enzymes. The S*XXX*H motif is highly conserved in AcpS enzymes from *Mycobacterium* and *Corynebacterium* species and is located in the vicinity of the CoA-binding pocket. In the *Mtb* apo-AcpS structure His49 (His65 in *C. ammoniagenes* AcpS) interacts with the sulfate ion. The present structural study also shows the participation of a second histidine in the active site. In *B. subtilis* AcpS the hydrophobic Phe49 residue occupies the place of His49 and does not contribute to active-site formation. The sequence alignment also shows that *C. ammoniagenes* AcpS has an insertion of 13 amino acids in the $\alpha2$–$\alpha3$ connecting loop.

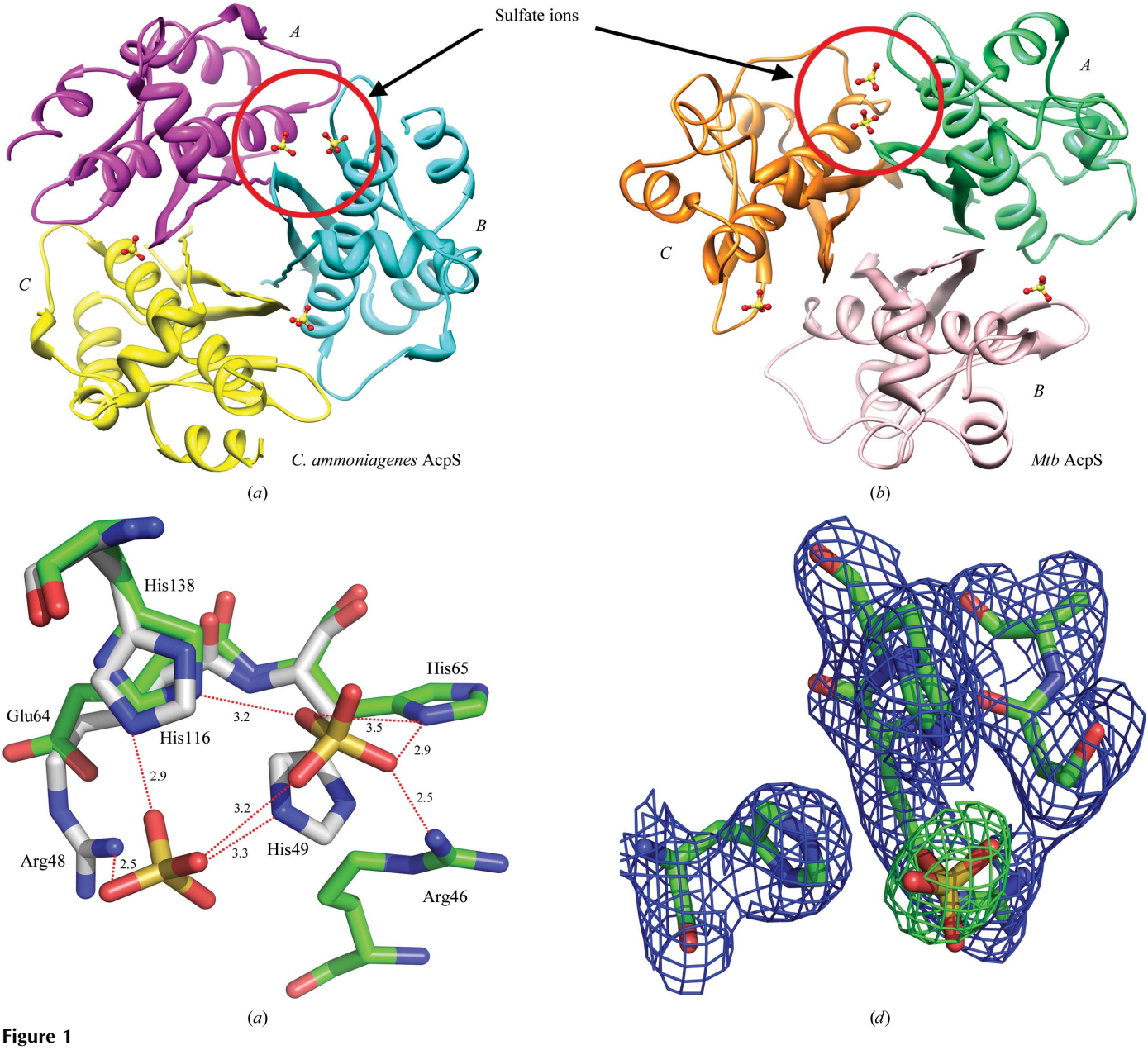

Figure 1
Overview of the *C. ammoniagenes* and *Mtb* AcpS structures with ribbon representation of the homotrimer. In the final model of the *C. ammoniagenes* AcpS structure each monomer contains residues 5–47 and 61–153. In the *Mtb* AcpS structure each monomer contains residues 2–130. The view is from the top of the trimer. (*a*) Ribbon diagram of the *C. ammoniagenes* AcpS homotrimeric structure: subunit *A* (magenta), subunit *B* (cyan) and subunit *C* (yellow). (*b*) Ribbon diagram of the *Mtb* AcpS homotrimer structure: subunit *A* (sea green), subunit *B* (plum) and subunit *C* (orange). The sulfate ion (shown in ball-and-stick representation) binds at the dimer interface, specifically in the cleft region that is formed by the two monomers. (*c*) Structural superposition of the *Mtb* and *C. ammoniagenes* AcpS active-site residues with sulfate ions. The bound sulfate ions are shown in stick representation. In *Mtb* AcpS His49 swings 101° compared with His65 of *C. ammoniagenes* AcpS. (*d*) Electron-density map of the substrate-binding pocket of *Mtb* AcpS. The carve feature in *PyMOL* was used to limit display of the electron density of the model. A $2F_o - F_c$ map contoured at 1.4σ (blue) and an $F_o - F_c$ map contoured at 4σ (green) are shown.

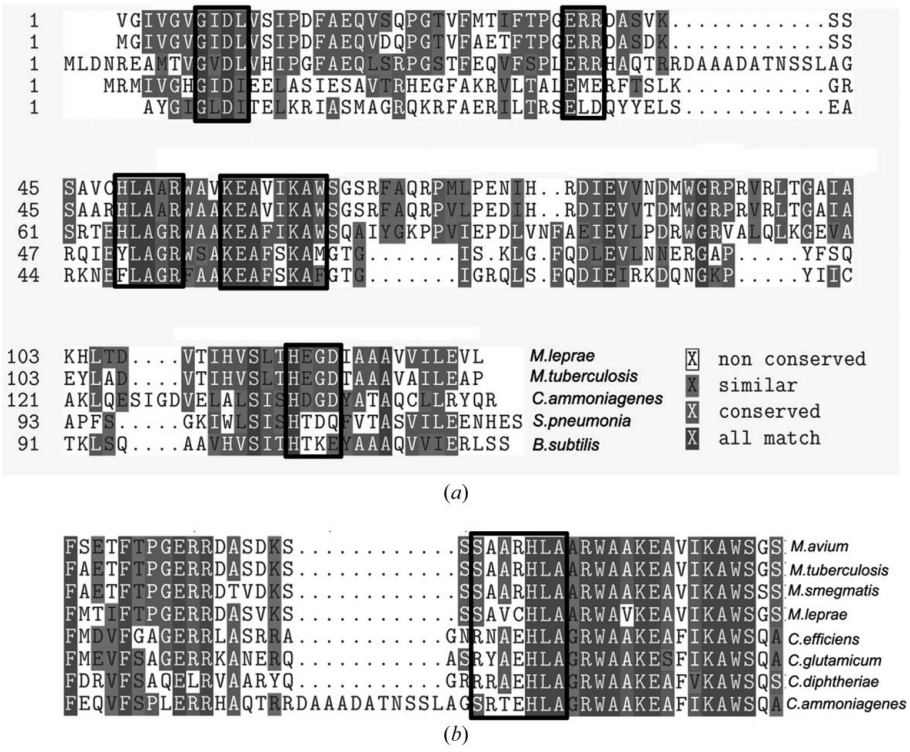

Figure 2
(*a*) Multiple sequence alignment of AcpS enzymes. The sequence alignment shows that *C. ammoniagenes* AcpS has an additional 12-residue (RDAAADATNSSL) insertion sequence between the α2 and α3 helices which is disordered in the structure. (*b*) Sequence alignment of AcpS enzymes from *Mycobacterium* and *Corynebacterium* species. The conserved S*XXX*HLA motif is shown in a box.

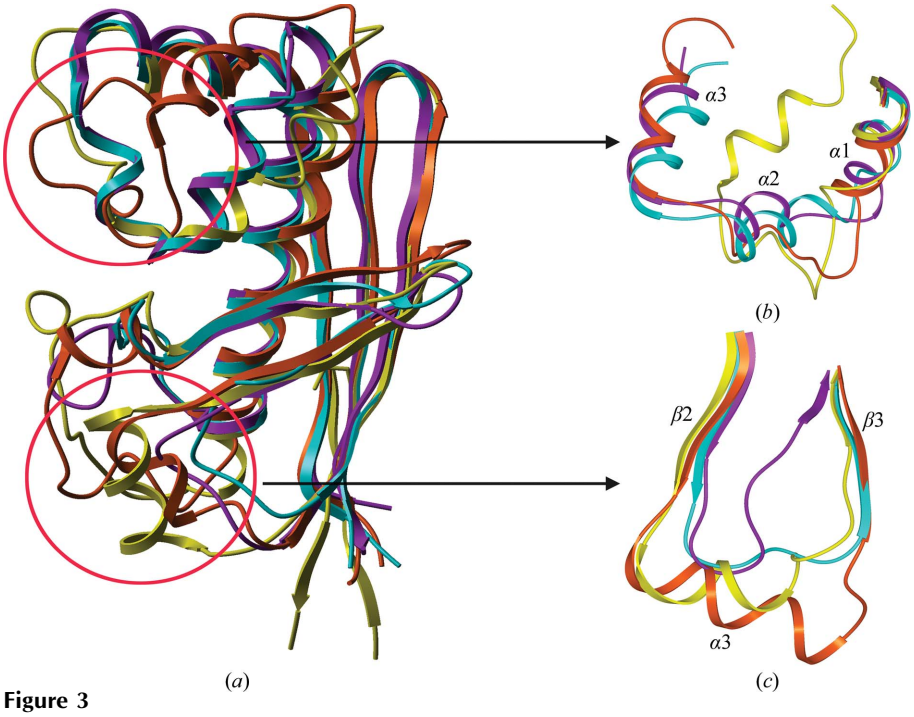

Figure 3
(*a*) Backbone superposition of the AcpS enzymes. Color key: orange, *Mtb*; yellow, *C. ammoniagenes*; cyan, *B. subtilis;* purple, *S. pneumoniae*. (*b*) The structural superposition reveals that the *B. subtilis* and *S. pneumoniae* AcpS structures have three short helices (α1, α2 and α3) between the β1 strand and the α3 'core' helix. The *Mtb* and *C. ammoniagenes* AcpS structures contain two short helices between β1 and the core helix. (*c*) The β2 and β3 strands of the *Mtb* and *C. ammoniagenes* AcpS structures are connected by a short helix which is absent in *B. subtilis* and *S. pneumoniae* AcpS.

Least-squares superposition of the structures indicate the close resemblance of *Mtb* AcpS and *C. ammoniagenes* AcpS to the *B. subtilis* and *S. pneumoniae* enzymes (r.m.s.d.s for 112 C^{α} atoms of ~1.67 and ~1.8 Å, respectively; Chirgadze *et al.*, 2000; Parris *et al.*, 2000; Figs. 3*a*–3*c*). In *B. subtilis* AcpS and *S. pneumoniae* AcpS three short α-helices (α1, α2 and α3) are located between the β1 strand and the long α4 helix (Fig. 3*b*). In contrast, in *C. ammoniagenes* AcpS and *Mtb* AcpS two short α-helices (α1 and α2) are located between the β1 strand and the long α3 helix (Fig. 3*b*). Structural alignment shows that the β1 strand and the α3 helix are connected by 30 residues in known AcpS structures. In the *Mtb* and *C. ammoniagenes* AcpS structures these 30 residues form two short α-helices (α1 and α2). In contrast, in the *S. pneumoniae* and *B. subtilis* AcpS enzymes the equivalent 30 residues (12–43) form three well ordered short α-helices (α1, α2 and α3). Because of the absence of one short α-helix (equivalent to α2 in *B. subtilis*), the connecting loop between the α1 and α2 helices is much larger and more flexible in the *Mtb* and *C. ammoniagenes* AcpS proteins. Furthermore, in *C. ammoniagenes* AcpS and *Mtb* AcpS the β3 and β4 strands are connected by a well defined α4 helix (residues 115–129 and 98–105, respectively; Fig. 3*c*), while in *B. subtilis* AcpS and *S. pneumoniae* AcpS the β3 and β4 strands are not connected by an α-helix but by a short loop (91–96). The topological rearrangements of the α-helix in *Mtb* AcpS and *C. ammoniagenes* AcpS may be required for their interactions with ACP, as *Mtb* AcpS and *C. ammoniagenes* AcpS are unusual members of the ACP family owing to their extended C-termini.

3.2. Structural differences between the open and closed structural forms of *Mtb* AcpS

A crystal structure of *Mtb* AcpS has recently been reported in which AcpS was crystallized in space group *P*23 and contained one molecule in the asymmetric unit (Dym *et al.*, 2009). The

reported AcpS–ADP structure is disordered in three regions (residues 22–30, 41–44 and 75–78) accounting for 13% of the AcpS model. *Mtb* apo-AcpS crystallized in space groups *I*222 and *R*3. Most notable was that in the *I*222 and *R*3 space groups AcpS had clear density for the entire model. AcpS crystallized as a homotrimer in space group *I*222, but in space group *R*3 it crystallized with a monomer in the asymmetric unit. The trimeric structure was maintained by the symmetry. The monomeric form was superimposed individually on chains *A*, *B* and *C* of the trimeric apo-AcpS structure with r.m.s.d.s of 0.91, 1.02 and 0.85 Å, respectively. Structural superposition of C^{α} atoms revealed that AcpS–ADP crystallized in space group

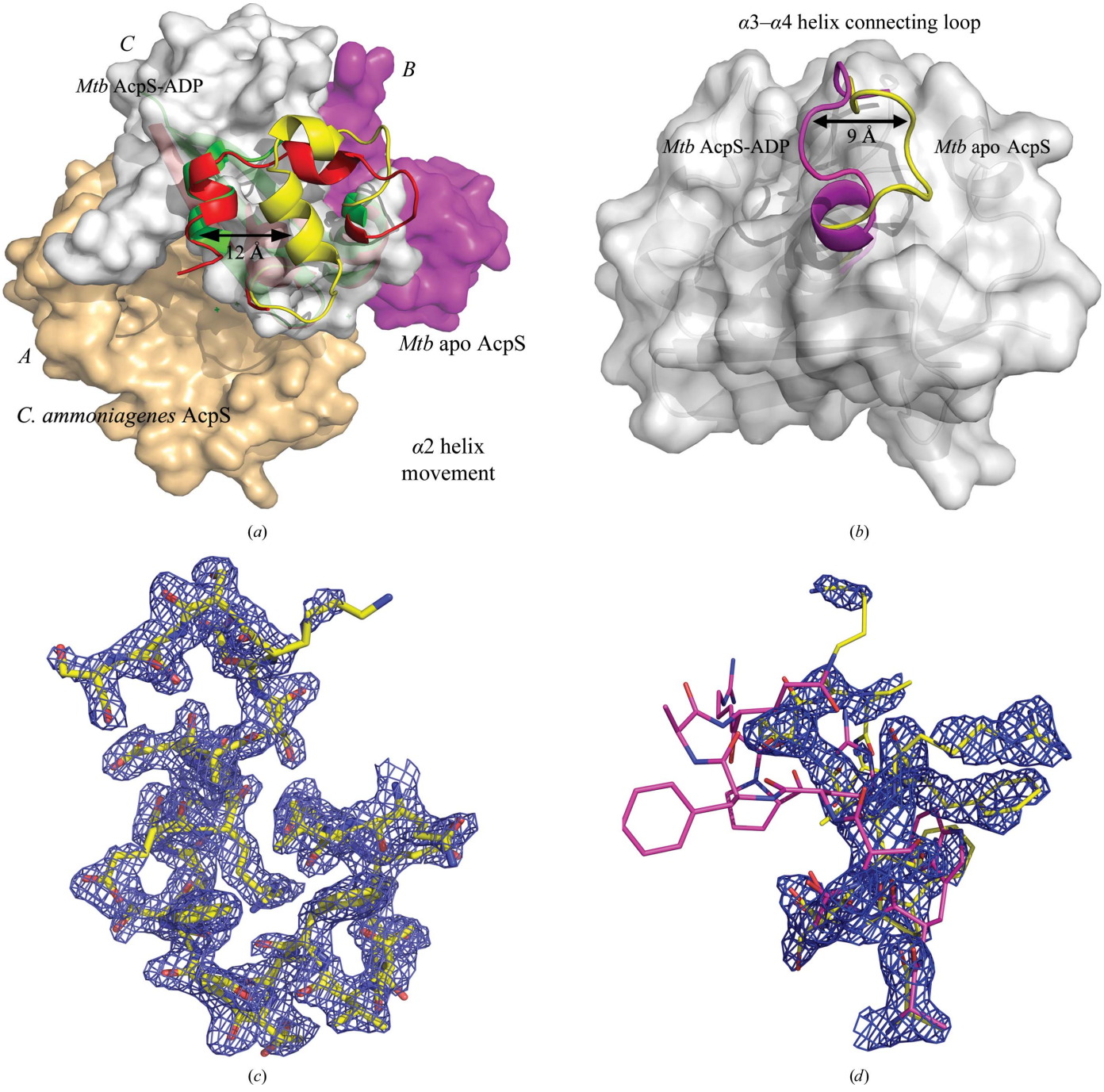

Figure 4
Overview of the α2-helix movement and the open and closed conformations of the α3–α4 connecting loop. (*a*) Structural superposition of helices α1, α2 and the connecting loop of the *Mtb* AcpS–ADP complex (green), *Mtb* apo-AcpS (yellow) and the *C. ammoniagenes* AcpS–CoA complex (red) represented by ribbon diagrams. *Mtb* apo-AcpS is shown as a surface representation; the surface of subunit *C* is shown partially in order to view the movement of the α2 helix at higher pH. (*b*) The α3–α4 connecting loop is shown in both the open and closed conformations. At higher pH values the α3–α4 connecting loop of the *Mtb* AcpS–ADP complex adopts an open conformation (purple). In the apo-AcpS structure (yellow) this same loop adopts a closed conformation. (*c*) Electron-density map of the *Mtb* apo-AcpS structure contoured at 1.4σ. At lower pH values the α1 and α2 helices are packed together; electron density is shown for residues 18–44. (*d*) Electron density for the α4 helix contoured at 1.4σ.

*P*23 retained an overall fold analogous to those of previously reported AcpS structures (Chirgadze *et al.*, 2000; Parris *et al.*, 2000). However, superposition of the C^{α} atoms reveals significant conformational changes of the C^{α} atoms in two regions, the α2 helix (residues 30–40; r.m.s.d. of 12 Å) and the connecting loop located between the α3 and α4 helices (residues 67–73; r.m.s.d. of 9 Å), when compared with the *Mtb* AcpS structure crystallized in space groups other than *P*23 (Figs. 4*a* and 4*b*). In contrast, the closed conformation was not observed in the *C. ammoniagenes* AcpS structure. The crystallographic data for *C. ammoniagenes* AcpS suggest that both the apo-AcpS and the AcpS–CoA complex structures adopt an open conformation. It is possible that in some cases crystal packing can contribute to the structural and conformational changes in the proteins. However, our current structural data show that *Mtb* AcpS crystallizes in three different space groups at lower pH and no structural changes were observed between them. In contrast, the structure of a crystals obtained at higher pH (unreported low-resolution data for apo-AcpS crystallized in space group *P*23, unit-cell parameters $a = b = c = 73.74$ Å, $\alpha = \beta = \gamma = 90.0^{\circ}$) superposes very well with the recently reported AcpS–ADP complex (Dym *et al.*, 2009). The crystals obtained at higher pH show three disordered regions and also structural movement in two regions. Taken together, these results suggest that the pH of the crystallization condition plays a significant role in the conformational changes of *Mtb* AcpS.

3.3. The effect of pH on the structure of the α2 helix

At lower pH values (between 4.4 and 6.0), the α1–α2 connecting loop is well ordered in the *Mtb* apo-AcpS structure. Residues from this loop make hydrogen-bonding interactions with residues in the α2 helix that result in close packing of the α1 and α2 helices on one side of the α3 or 'core' helix. Likewise, residues from helix α2 interact with residues from helix α3. In particular, the distance between the hydroxyl group of Thr25 and the main-chain N atom of Phe27 is 3.06 Å and the guanidinium group (NH1) of Arg53 from the α3 helix interacts with the acidic side chain of Glu35 (OE2) from the α2 helix (3.19 Å) at low pH. At higher pH values the AcpS structure undergoes a significant conformational change in which the α2 helix moves 12 Å away from the α1 helix and occupies a position close to the antiparallel β2 and β3 strands (Fig. 4*a*). The rearrangement of the α2 helix also leads to the destabilization of the connecting loops at both ends, resulting in disordered electron density for residues 21–30 and 41–44. This movement increases the flexibility of the connecting loop, thereby altering the hydrogen bonds and hydrophobic interactions with the α2 helix as well as the ionic interaction between the α2 and α3 helices. The ionic interaction between the Glu35 and Arg53 residues is lost; instead, the side chain of Arg53 interacts with the phosphate group of ADP. Superposition of the higher pH structure of *Mtb* apo-AcpS with that of *C. ammoniagenes* AcpS–CoA shows that the Arg69 residue and the *Mtb* Arg53 residue overlay each other. It is clear that the ionic interaction is lost as a consequence of the change in pH and not the ligand binding.

3.4. Open and closed conformations of the connecting loop between helices α3 and α4

Structure-based sequence alignment revealed that the connecting loop between helices α3 and α4 of *Mtb* AcpS contains six additional residues compared with the known AcpS structure, resulting in the loop adopting an open conformation (Fig. 4*b*; Dym *et al.*, 2009). In our structure, the α3–α4 connecting loop adopts a closed conformation despite the presence of the additional six residues (Fig. 4*b*). The pH of the conditions used for crystal growth is the only difference between these two structures. At lower pH values (4.4–6.0) the α3–α4 connecting loop adopts a closed conformation. Structural superposition reveals that the closed conformation of *Mtb* AcpS is similar to those in the structures of AcpS from *B. subtilis* (Parris *et al.*, 2000) and *S. pneumoniae* (Chirgadze *et al.*, 2000). These results indicate that the α3–α4 connecting loop adopts two different conformations based on the pH of the crystallization conditions. The r.m.s.d. value of the individual residues of the α3–α4 connecting loop of AcpS at pH 6.5 compared with the low-pH structure is approximately 6 Å. At lower pH values, the α3–α4 connecting loop points towards the connecting loop between the α3 helix and the β2 strand of the same subunit. The Phe69 side chain is buried in the hydrophobic pocket formed by Val4, Leu105, Val108 and Ala129. At higher pH values, residues 68–72 flip 150° in the opposite direction and move towards the connecting loop between the β2 and β3 strands of the neighboring subunit. In the open conformation, the Phe69 residue shows the largest deviation (the r.m.s.d. of the C^{α} atom is 9.6 Å), followed by Ala70 (the r.m.s.d. of the C^{α} atom is 9.2 Å), when compared with the closed conformation (Figs. 4*b* and 4*d*).

Dym and coworkers postulated that in *C. ammoniagenes* AcpS the α3–α4 connecting loop will adopt an open conformation as in the *Mtb* AcpS–ADP complex structure owing to their sequence conservation and identity (Dym *et al.*, 2009). Here, we report the crystal structure of *C. ammoniagenes* AcpS with and without CoA. Both apo-AcpS and AcpS–CoA crystallized as homotrimers and superimposed very well (r.m.s.d. of 0.45 Å). Superposition of the *Mtb* apo-AcpS structure with the *C. ammoniagenes* AcpS structure (apo-AcpS and AcpS–CoA) shows that the α2 helix (residues 33–43) moves 12 Å towards the β2 and β3 strands and the α3–α4 connecting loop (residue 82–88) undergoes a conformational change resembling the open structure of the *Mtb* AcpS–ADP structure. The open and closed conformations of AcpS cannot be correlated with complex formation but rather with changes in pH.

Another unexpected observation is that a portion of the α4 helix (residues 73–78) is disordered in the *Mtb* AcpS–ADP complex. It has been hypothesized that this loop (74–78) may be stabilized by the interaction of AcpS with AcpM. In contrast, the pH 5.3 crystal structure of *Mtb* AcpS and the pH 6.5 crystal structure of *C. ammoniagenes* AcpS exhibit

electron density for all of the backbone and side-chain residues of the α4 helix (Fig. 4*d*). This suggests that the interaction between AcpM and AcpS is not required for stabilization of the α4 helix of AcpS. In the lower-pH AcpS structure the connecting loops and the α4-helix region have higher *B* factors in comparison with the remaining region, indicating that these regions are highly flexible and are beginning to undergo conformational change. This pH-induced conformational change in AcpS may provide insight into a possible mechanism of protein–protein interaction. At higher pH values the Arg48 and His49 residues of the α3 helix do not participate in the CoA-binding mechanism; these residues are highly conserved in AcpS enzymes from *Mycobacterium* species. In contrast, at low pH these two residues actively participate in sulfate binding in the apo structure of *Mtb* AcpS (Figs. 1*c* and 1*d*). Similarly, in *C. ammoniagenes* the equivalent residues (Glu64 and His65) participate in both sulfate and CoA binding. The His65 residue is highly conserved in *Corynebacterium* AcpS enzymes; it is located in the active site and forms a hydrogen bond to the phosphate group of CoA (Fig. 2*c*). AcpS crystallized in space group *P*23 does not show an interaction with the second histidine in the sulfate/CoA-binding mechanism.

3.5. Active site of the apo-AcpS structure

The active sites of *Mtb* AcpS and *C. ammoniagenes* AcpS are formed at the interface of the trimer. Electron density for a sulfate ion is visible in the unbiased electron-density maps of both the *Mtb* and *C. ammoniagenes* AcpS native structures (Fig. 1*d*). The locations of the identified sulfate ions are adjacent to a series of well conserved residues, specifically Arg48, His49 and His116 in *Mtb* AcpS, and Arg46, Glu64, His65 and His138 in *C. ammoniagenes* AcpS. These sulfate ions are associated with residues found in the CoA-binding pocket identified in the *B. subtilis* AcpS structure (Parris *et al.*, 2000). The sulfate ion occupies the same position as the 3′-phosphate of CoA. Previous studies have shown that the active sites of *S. pneumoniae* AcpS are occupied by sulfate ions (Chirgadze *et al.*, 2000). Of particular interest are the two O atoms (O1 and O2) of the sulfate that form hydrogen bonds to Arg48 NH1 (distances of 2.48 and 2.89 Å, respectively) of subunit *A*. The guanidinium group of Arg48 is at a favorable distance to form a hydrogen bond to the carbonyl groups of the highly conserved Ser43 (3.01 Å; Fig. 1*d*). O atoms O1 and O3 of the sulfate ion also form hydrogen bonds to NE2 of His49 and His116 (2.82 Å), respectively. Of the three active sites, two contained one sulfate ion and one was occupied by two sulfate ions. A similar result was also observed in the *C. ammoniagenes* apo-AcpS structure (Figs. 1*a* and 1*b*). In *C. ammoniagenes* AcpS the Glu64 residue is replaced by Arg48, which occupies an identical location as in the *Mtb* AcpS structure. However, the location and orientation of His65 and the sulfate ion in the active site of the *C. ammoniagenes* AcpS structure are not identical to their positions in *Mtb*. This can be explained in two ways. Firstly, in *C. ammoniagenes* AcpS the His65 and His138 residues are surrounded by Glu64 on one side and Arg46 on the other. Owing to the negative charge of Glu69 the sulfate ion is located in a favorable position to interact with the basic residue Arg46. Secondly, owing to the long side chain of Arg48 the sulfate ions occupy a different location in *Mtb* AcpS, making the side chain of His49 swing approximately 101° compared with His65 of *C. ammoniagenes* AcpS and facilitating interaction with the sulfate ion (Fig. 1*c*). Nevertheless, the structural data clearly indicate that in the absence of CoA the active sites are occupied by sulfate ions.

3.6. The binary complex of AcpS and CoA

The CoA-bound *C. ammoniagenes* AcpS structure was solved by molecular replacement. This binary complex crystallized in space group *P*1 and contained six monomers arranged as two groups of trimers. In the AcpS–CoA complex density for ADP was very clear in each binding site and allowed unambiguous positioning of ADP. Superposition of the carbon backbone of native AcpS with the ADP-bound binary complex reveals that binding of CoA does not alter the structural conformation of the biological unit. The adenine ring of ADP fits between the β2 and β3 loops, consisting of residues 108–112 of subunit *A* and residues 81–86 of subunit *B* of the AcpS trimer. The adenine base is immobilized by a network of interactions created by Ser81, Trp108 and Gly109 (Fig. 5). The ribose is present in the 3′-*endo* conformation, with axial orientation of the 2′-hydroxyl group and equatorial orientation of the 3′-phosphate group. The 3′-phosphate group of ADP is bound tightly to the protein through a number of interactions, specifically with the imidazole rings of His65 and His138, and His46 and Arg69 make contacts with the 3′-phosphate through a water molecule. The 5′-α-phosphate is packed against the β1 strand and the α3 helix of the second molecule and is positioned within hydrogen-bonding distance of the main chain of His105, the N^{ε} group of Lys78 and the hydroxyl group of Ser137. The 5′-β-phosphate group of CoA

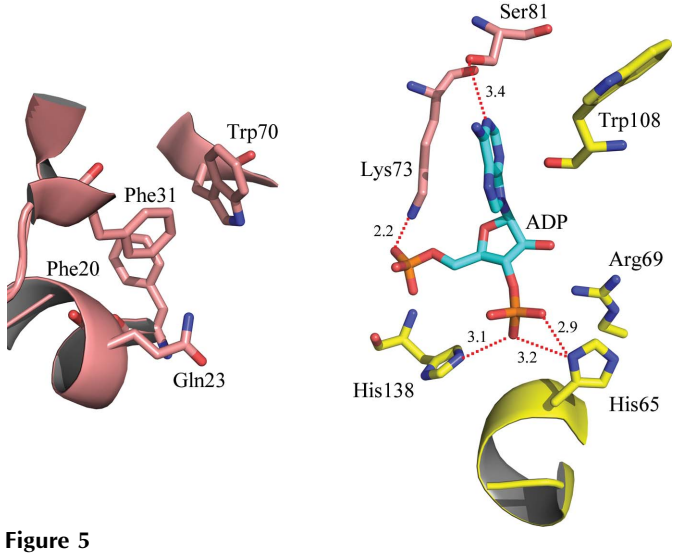

Figure 5
ADP binds in the dimer interface between two subunits. The active-site residues of one subunit are colored yellow, those of the second subunit are colored salmon and ADP is colored cyan.

does not interact with any of the protein residues. The 4′-ppt arm and the β-mercaptoethanol-binding pocket extend away from the adenine base and are surrounded by mostly hydrophobic residues, specifically Ile77*B*, Pro93*B*, Phe98*B* and Trp108*A*. The involvement of the imidazole rings of His65 and His138 in CoA binding probably contributes to the strict pH-dependence of AcpS activity.

3.7. *Mtb* AcpS can selectively transfer BODIPY-labeled CoA to *Mtb* apo-ACP

The activity of *Mtb* AcpS in post-translational modification of apo-ACP was assessed. We incubated recombinant *Mtb* AcpS with BODIPY-labeled CoA (a fluorescent dye is attached to the sulfhydryl group of CoA) and apo-ACP and an aliquot of the reaction was analyzed by SDS–PAGE. When the SDS gel was viewed under a UV illuminator, the post-translationally modified holo-ACP was visualized as a fluorescent band with the expected molecular size. The fluorescent SDS gel clearly demonstrated that *Mtb* AcpS was able to transfer the 4′-phosphopantetheine arm to ACP upon incubation with BODIPY-CoA and *Mtb* apo-ACP. We used two different concentrations of AcpS, 0.2 and 2 µ*M*, and the fluorescence intensity of holo-ACP clearly showed that AcpS effectively transfers the 4′-phosphopantetheine arm to apo-ACP even at 0.2 µ*M* (Fig. 6*a*). Similarly, AcpS was pre-incubated with unlabeled CoA and then assessed for post-translational modification activity in the presence of BODIPY-CoA and apo-ACP. The result shows that the fluorescence intensity decreases upon pre-incubation with CoA, as part of the holo-ACP contains nonfluorescent 4′-phosphopantetheine and part contains fluorescent BODIPY-4′-phosphopantetheine (Fig. 6*a*). Owing to the heterogeneous population, diminished florescence intensity was observed in the CoA pre-incubation experiment.

Next, we assessed the specificity of the AcpS post-translational modification activity. PKS11 was used as a negative control since it is not a substrate of AcpS *in vivo*. In this experiment, we incubated *Mtb* AcpS with BODIPY-labeled CoA and *Mtb* PKS11 in order to determine whether AcpS is able to transfer 4′-ppt to PKS11 (as this protein has a malonyl-CoA-binding tunnel). *Mtb* AcpS was unable to transfer the 4′-ppt moiety to PKS11 despite the presence of a CoA-binding tunnel, which demonstrates the specificity of AcpS. This experiment shows that *Mtb* AcpS is functionally active and is able to convert apo-ACP to holo-ACP. The crystal structure reveals that *Mtb* AcpS adopts one conformation at low pH and a different conformation at higher pH. This led us to assess the post-translational modification activity of AcpS at different pH values from 3.4 to 8.0. The fluorescence SDS gel clearly shows that AcpS is unable to transfer the 4′-ppt arm to ACP at lower pH values (3.4–4.0), but it is able to transfer the 4′-ppt arm to ACP at pH 4.4–8.0. However, the relative florescence intensity was higher between pH 4.4 and 6.0 compared with pH 6.6–8.0 (Fig. 6*b*). Recently, the *Mtb* FAS-I enzyme has been expressed and purified from *E. coli* and a reconstitution experiment showed that the FAS-I enzyme was inactive. In contrast, co-expression of the *Mtb* FAS-I enzyme with *Mtb* AcpS (in a duet vector) resulted in a FAS-I enzyme which was biochemically active (Qingan & Sacchettini, unpublished work). During co-expression, *Mtb* AcpS post-translationally modifies the ACP domain of the FAS-I enzyme *via* a CoA-derived 4′-ppt group. It is evident that AcpS modifies the ACP domain of FAS-I as well as AcpM.

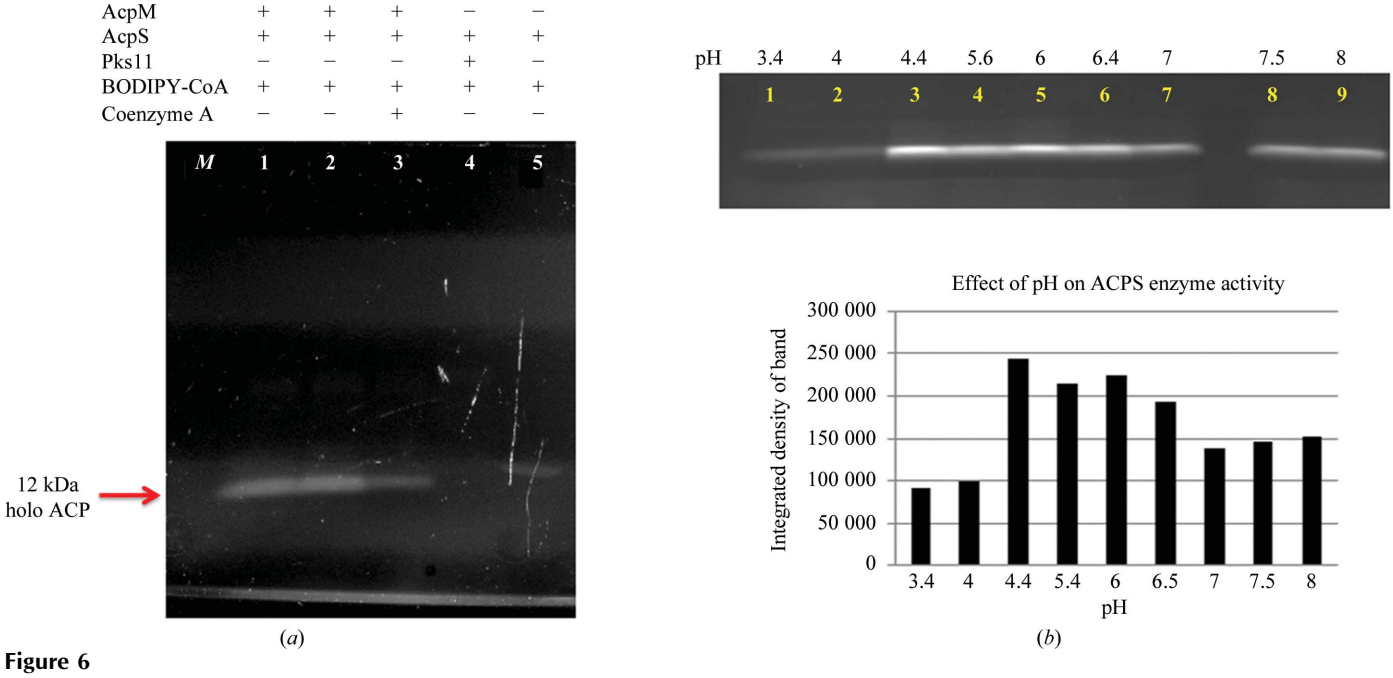

Figure 6
AcpS post-translational modification activity assay. (*a*) Lane *M*, molecular-weight markers; lane 1, 0.2 µ*M* AcpS; lane 2, 2 µ*M* AcpS; lane 3, pre-incubation of AcpS with CoA; lane 4, incubation with PKS11; lane 5, incubation of AcpS and BODIPY-CoA alone. (*b*) *Mtb* AcpS activity was assessed from pH 3.4 to pH 8.0. The intensities are shown in the bar diagram.

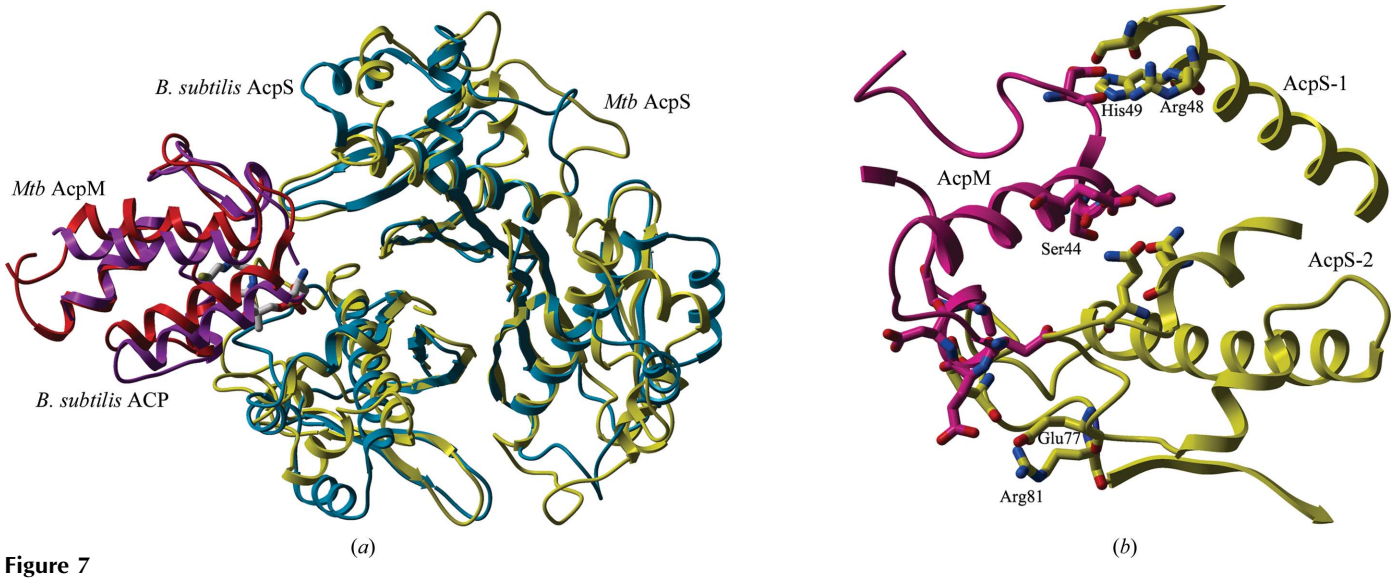

Figure 7
(*a*) Structural superposition of AcpS–holo-ACP from *B. subtilis* with *Mtb* AcpS and the solution structure of AcpM. (*b*) The interacting residues of *Mtb* AcpS and AcpM are shown as stick models. ACP occupies the space between the dimer interface and S*XXX*H in a favorable position to interact with ACP.

3.8. Comparison of the *B. subtilis* AcpS–ACP complex with a proposed model of the *Mtb* AcpS–AcpM complex

ACP is a key component in both fatty-acid biosynthesis and polyketide biosynthesis. Initially, ACP is post-translationally modified by AcpS. During this process, AcpS recognizes the conserved Asp-Ser-Leu motif in apo-ACP and transfers the 4′-ppt moiety from CoA to a serine residue. The crystal structure of the *B. subtilis* AcpS–holo-ACP complex has been reported (Parris *et al.*, 2000). In *B. subtilis* the Arg14, Arg21, Arg22 and Arg28 residues of AcpS interact with the Asp38 and Glu46 acids of holo-ACP. Multiple sequence alignments indicate that *Mtb* AcpS does not contain an Arg residue in the N-terminal region (residues 14, 21, 22 and 28); rather, it contains Asp, Gln and Glu in place of Arg (Fig. 7*a*). *C. ammoniagenes* AcpS has similar residues to those of *Mtb* AcpS, with the exception of the Arg22 residue. In contrast, the ACP amino-acid sequence alignment indicates that the EKS, DED and IPDED motifs and the 4′-ppt-binding motif (DSL) are highly conserved in all bacteria. In *B. subtilis*, the conserved residues of ACP interact with AcpS. In order to understand the interaction between AcpS and AcpM in *Mtb*, we superimposed the *Mtb* AcpS structure (the current model) and the AcpM NMR structure (PDB entry 1klp; Wong *et al.*, 2002; residues 1–90) with the *B. subtilis* AcpS–holo-ACP complex structure (Fig. 7*a*). The superimposed model of the AcpS–holo-ACP complex was energy-minimized using the *Discovery* III suite of the *INSIGHT* II software. The complex shows that the location and orientation of *Mtb* ACP are very similar to those of *B. subtilis* ACP; however, the interacting residues are different. Specifically, Glu19, Gln22, Ser45, Arg48, His49, Glu77 and Arg81 of AcpS are responsible for *Mtb* ACP binding. In particular, AcpS residues Ser45, Arg48 and His49 are close enough to interact with Asp38 of ACP (Fig. 7*b*). The conserved IPDED motif of ACP is sufficiently near to form a hydrogen-bonding network with Glu77 and Arg81 of AcpS. Another conserved residue, Asp46, of ACP is close enough to interact with Glu19 and Gln22 of AcpS. The minimized AcpS–AcpM model shows that Arg48 and His49 of AcpS are at a favorable distance to interact with AcpM residues in addition to binding CoA or ADP. This model contains residues 1–90 of ACP but does not address the role of the C-terminal region of ACP and its interaction with AcpS. We are currently working to produce an ACP–AcpS complex to answer these questions.

4. Conclusions

We have determined the structures of both apo-AcpS and AcpS in complex with CoA from *Mtb* and *C. ammoniagenes* and have found that AcpS adopts different pH-dependent conformations. The active sites of the apo-AcpS and CoA-bound AcpS structures show that His49 and His116 (His65 and His136 in *C. ammoniagenes*) participate in either sulfate binding or CoA binding. The fluorescence assay demonstrates the functionality of AcpS, which converts apo-ACP to holo-ACP. The structural differences observed between *Mtb* AcpS and *C. ammoniagenes* AcpS may be essential for interaction with ACP. Finally, the structural basis of AcpS–ACP interactions in the *Corynebacterium* subgroup is fundamentally different from the electrostatic complementarity found in other bacterial systems.

This work was supported by the following grants: Structural Genomics of Persistence Targets from *Mycobacterium tuberculosis* (PO1AI068135) and the R. J. Wolfe-Welch Foundation Chair in Science (8-0015). We appreciate the support of staff scientists at beamlines 14-ID and 19-ID of the Advanced Photon Source, Argonne National Laboratory for their help with data collection. We also thank Stephanie Swanson and

Bhavini Patel for excellent technical assistance and Tracey Musa for comments on the manuscript. GSB acknowledges support in the form of a Personal Research Chair from Mr James Bardrick, Royal Society Wolfson Research Merit Award, as a former Lister Institute–Jenner Research Fellow, and the Medical Research Council.

References

Baldwin, J. E., Bird, J. W., Field, R. A., O'Callaghan, N. M., Schofield, C. J. & Willis, A. C. (1991). *J. Antibiot.* **44**, 241–248.
Bricogne, G., Vonrhein, C., Paciorek, W., Flensburg, C., Schiltz, M., Blanc, E., Roversi, P., Morris, R. & Evans, G. (2002). *Acta Cryst.* A**58**, C239.
Chalut, C., Botella, L., de Sousa-D'Auria, C., Houssin, C. & Guilhot, C. (2006). *Proc. Natl Acad. Sci. USA*, **103**, 8511–8516.
Chirgadze, N. Y., Briggs, S. L., McAllister, K. A., Fischl, A. S. & Zhao, G. (2000). *EMBO. J.* **19**, 5281–5287.
Cole, S. T. *et al.* (1998). *Nature (London)*, **393**, 537–544.
Dubey, V. S., Sirakova, T. D., Cynamon, M. H. & Kolattukudy, P. E. (2003). *J. Bacteriol.* **185**, 4620–4625.
Dym, O., Albeck, S., Peleg, Y., Schwarz, A., Shakked, Z., Burstein, Y. & Zimhony, O. (2009). *J. Mol. Biol.* **393**, 937–950.
Geiger, O., Spaink, H. P. & Kennedy, E. P. (1991). *J. Bacteriol.* **173**, 2872–2878.
Hendrickson, W. A. (1991). *Science*, **254**, 51–58.
Hendrickson, W. A. & Ogata, C. M. (1997). *Methods Enzymol.* **276**, 494–523.
Issartel, J. P., Koronakis, V. & Hughes, C. (1991). *Nature (London)*, **351**, 759–761.
Kantardjieff, K. A., Höchtl, P., Segelke, B. W., Tao, F.-M. & Rupp, B. (2002). *Acta Cryst.* D**58**, 735–743.
Kissinger, C. R., Gehlhaar, D. K. & Fogel, D. B. (1999). *Acta Cryst.* D**55**, 484–491.
La Clair, J. J., Foley, T. L., Schegg, T. R., Regan, C. M. & Burkart, M. D. (2004). *Chem. Biol.* **11**, 195–201.
La Fortelle, E. de & Bricogne, G. (1997). *Methods Enzymol.* **276**, 472–494.
Lambalot, R. H. & Walsh, C. T. (1995). *J. Biol. Chem.* **270**, 24658–24661.
Magnuson, K., Jackowski, S., Rock, C. O. & Cronan, J. E. (1993). *Microbiol. Rev.* **57**, 522–542.
Matthews, B. W. (1968). *J. Mol. Biol.* **33**, 491–497.
McAllister, K. A., Peery, R. B., Meier, T. I., Fischl, A. S. & Zhao, G. (2000). *J. Biol. Chem.* **275**, 30864–30872.
McPherson, A. (1982). *Preparation and Analysis of Protein Crystals*. New York: John Wiley & Sons.
McRee, D. E. (1999). *J. Struct. Biol.* **125**, 156–165.
Murshudov, G. N., Skubák, P., Lebedev, A. A., Pannu, N. S., Steiner, R. A., Nicholls, R. A., Winn, M. D., Long, F. & Vagin, A. A. (2011). *Acta Cryst.* D**67**, 355–367.
Otwinowski, Z. & Minor, W. (1997). *Methods Enzymol.* **276**, 307–326.
Parris, K. D., Lin, L., Tam, A., Mathew, R., Hixon, J., Stahl, M., Fritz, C. C., Seehra, J. & Somers, W. S. (2000). *Structure Fold. Des.* **8**, 883–895.
Rock, C. O. & Cronan, J. E. (1996). *Biochim. Biophys. Acta*, **1302**, 1–16.
Sheldrick, G. M. (2008). *Acta Cryst.* A**64**, 112–122.
Shen, B., Summers, R. G., Gramajo, H., Bibb, M. J. & Hutchinson, C. R. (1992). *J. Bacteriol.* **174**, 3818–3821.
Smith, S. (1994). *FASEB J.* **8**, 1248–1259.
Taylor, R. C., Brown, A. K., Singh, A., Bhatt, A. & Besra, G. S. (2010). *Microbiology*, **156**, 1975–1982.
Terwilliger, T. C. & Berendzen, J. (1999). *Acta Cryst.* D**55**, 849–861.
Wong, H. C., Liu, G., Zhang, Y.-M., Rock, C. O. & Zheng, J. (2002). *J. Biol. Chem.* **277**, 15874–15880.